Theor Chem Acc (1998) 100:134–146
DOI 10.1007/s002149800m59

Theoretical
Chemistry Accounts

Regular article

A theoretical study of the acetylide anion, HCC^-*

Mirjana Mladenović[1], Peter Botschwina[1], Peter Sebald[2], Stuart Carter[3]

[1] Institut für Physikalische Chemie, Universität Göttingen, Tammannstrasse 6, D-37077 Göttingen, Germany
[2] Fachbereich Chemie der Universität Kaiserslautern, Erwin-Schrödinger-Strasse, D-67663 Kaiserslautern, Germany
[3] Department of Chemistry, University of Reading, Reading RG6 2AD, UK

Received: 27 July 1998 / Accepted: 12 August 1998 / Published online: 19 October 1998

Abstract. The results of various ab initio calculations are reported for the electronic ground state of the acetylide anion. An "Eyring's lake" in the T-shaped configuration is identified with six different methods (SCF, MP2, CCSD, CCSD-T, CCSD(T), and CEPA–1). The equilibrium bond lengths of HCC^- are estimated to be $r_e(CH) = 1.0689(3)$ Å and $R_e(CC) = 1.2464(2)$ Å, and the ground-state rotational constant is predicted to be $B_0 = 41636(20)$ MHz. The large permanent dipole moment of $\mu_0 = -3.093$ D should facilitate detection of the anion by microwave spectroscopy. The band centers are predicted to be 3211.3 cm^{-1}(ν_1), 511.1 cm^{-1}(ν_2), and 1805.0 cm^{-1}(ν_3). A large transition dipole moment of 0.477 D is calculated for the ν_2 band. Rovibrational levels of HCC^- up to approximately 20 000 cm^{-1} above equilibrium are calculated with DVR-DGB and FBR methods on the basis of a previous CEPA–1 potential energy surface. Different energy patterns are found and discussed, for which anharmonic and Coriolis resonances are shown to play an important role.

Key words: HCC^- – Rovibrational states – Coriolis resonances – Barrier height to isomerization – Spectroscopic properties – Negative ions

1 Introduction

Although the acetylide anion, HCC^-, is one of the fundamental organic anions and a rather abundant species in hydrocarbon flames (see, e.g., Ref. [1]), very little spectroscopic information exists for the free anion in the gaseous phase. In particular, a high-resolution study of the anion in any wavelength region is still missing. In 1987, Gruebele et al. [2] claimed to have observed 12 lines of the CC stretching rovibrational band (ν_3) of HCC^- by means of diode laser infrared spectroscopy. On the basis of ab initio calculations within the coupled electron-pair approximation (CEPA) [3, 4], the assignments were immediately heavily critized by one of us [5, 6]. Both the band origin and, even much more pronounced, the vibration-rotation coupling constant α_3 were in intolerable disagreement with the results of the ab initio calculations. The ν_3 band origin was calculated to be 1815.5 cm^{-1} (CEPA–1) and, by transferring a correction from acetylene, a value of 1807 ± 5 cm^{-1} was recommended [6]. This theoretical prediction was experimentally confirmed by Ervin and Lineberger [7]. They observed a hot band in the photoelectron spectrum of HCC^- which originated from the $\nu_3 = 1$ vibrational state and they determined ν_3 to be 1800 ± 20 cm^{-1}.

The CEPA calculations were extended by Sebald and Botschwina [8, 9] who constructed a 3D potential energy function (PEF) capable of describing highly excited vibrational states and, for the first time, found a shallow energy minimum (some sort of an "Eyring's lake") in a T-shaped configuration of the nuclei. This feature of the potential energy surface (PES) was found later in less extensive calculations by Tian et al. [10] and was confirmed through extended coupled-cluster calculations [11, 12]. In addition, absolute infrared intensities of pure stretching vibrational transitions were calculated within a 2D anharmonic approximation [13].

The purpose of the present paper is twofold. Firstly, we will present the results of new coupled-cluster calculations which should reliably predict the ν_1 (∼CH stretch) and ν_2 (bend) band origins with an uncertainty of about 2 cm^{-1} and the ν_3 band origin with an uncertainty of about 5 cm^{-1}. In addition, we aim to predict the ground-state rotational constant within an uncertainty of about 0.05%. The calculated ground-state electric dipole moment should be accurate to better than 0.01 D and the calculated vibrational transition moments for the fundamental bands are expected to have uncertainties of less than 2%.

* Dedicated to Prof. Dr. Wilfried Meyer on the occasion of his 60th birthday

Correspondence to: P. Botschwina

Secondly, we make use of the previous, quite accurate CEPA–1 potential [8, 9] in a detailed investigation of higher excited rovibrational states, with particular emphasis on states lying in the energy regime of the saddle points to H migration and the T-shaped local energy minimum. In this region, a transition takes place between regular vibrational states and rotor-like states, with an intermediate group of levels in between.

2 A near-equilibrium CCSD(T) PES for HCC^- and predictions of spectroscopic properties

The coupled-cluster variant CCSD(T) [14] was employed in the calculation of a near-equilibrium PEF for HCC^- which covers an energy range of about $10\,000\,cm^{-1}$ above linear equilibrium. All electrons were correlated in the CCSD(T) calculations, which were carried out with the MOLPRO suite of programs [15]. A basis set of 250 contracted Gaussian-type orbitals (CGTOs) was employed which consists of the *s*, *p*, and *d* part of the correlation-consistent core plus valence quadruple zeta (cc-pCVQZ) set of Woon and Dunning [16] for carbon. It was augmented by the corresponding "diffuse" functions from the aug-cc-pVQZ set [17] plus the full sets of *f* and *g* functions from the same basis. The full aug-cc-pVQZ hydrogen basis was used. An analytical PEF in standard polynomial form was obtained through a least-squares fit to 130 calculated energy points which, after transformation to equilibrium, reads

$$V - V_e = \sum_{ijk} C_{ijk} \Delta r^i \Delta R^j \alpha^k \quad (k: \text{even}) \tag{1}$$

Here, Δr and ΔR denote the changes of the CH and CC internuclear separations with respect to their equilibrium values and the angle α measures the deviation from linearity. The equilibrium bond lengths were calculated to be $r_e(CH) = 1.0697$ Å and $R_e(CC) = 1.2474$ Å. The same sort of calculation for isoelectronic HCN yields $r_e(CH) = 1.0658$ Å and $R_e(CC) = 1.1542$ Å, compared with the currently best experimental values of 1.06501(8) and 1.15324(2) Å [18]. Assuming the same errors in the CCSD(T) calculations hold for HCC^-, we arrive at $r_e(CH) = 1.0689(3)$ Å and $R_e(CC) = 1.2464(2)$ Å, with estimated error bars in parentheses. These values are in excellent agreement with our previous predictions of 1.0696(5) and 1.2463(10) Å [6]. We have also carried out analogous CCSD(T) calculations for acetylene and obtained $r_e(CH) = 1.0623$ Å and $R_e(CC) = 1.2041$ Å. Solely on the basis of experimental data, the equilibrium structure of HCCH is still not too well-established, and we therefore favor our previous recommended structure [CCSD(T) results plus corrections] of $r_e(CH) = 1.0617(5)$ Å and $R_e(CC) = 1.2032(2)$ Å [19]. The differences between the present CCSD(T) results and this structure are $\Delta r_e = 0.0006$ Å and $\Delta R_e = 0.0009$ Å, and are thus very similar to those of HCN.

The PEF coefficients C_{ijk} for HCC^- are listed in Table 1. A plot of the relatively shallow HCC bending potential is compared with the corresponding potentials of HCN [20] and HCO^+ [21] in Fig. 1. In the case of the latter two species, the complete cc-pCVQZ basis set (198 CGTOs) was employed in the calculations.

An electric dipole moment function was calculated around the present CCSD(T) equilibrium geometry, making use of the aug-cc-pVQZ basis and restricting the correlation treatment to the valence electrons in CCSD(T) calculations. Dipole moments were calculated as energy derivatives. The resulting values were transformed locally, that is for each nuclear configuration, to the Eckart coordinate system [22]. Parallel and perpendicular components of the dipole moment vector were then fitted separately according to

$$\mu^{\parallel} - \mu_e = \sum_{ijk} D^{\parallel}_{ijk} \Delta r^i \Delta R^j \alpha^k \ , \tag{2}$$

Table 1. Coefficients C_{ijk} (in a.u.) of the CCSD(T) potential energy function (PEF) for HCC^- [a]

i	*j*	*k*	C_{ijk}	*i*	*j*	*k*	C_{ijk}
2	0	0	0.1931997	0	0	2	0.0155532
3	0	0	−0.1983988	0	0	4	0.0021789
4	0	0	0.1325729	0	0	6	−0.0011442
5	0	0	−0.0771111	0	0	8	0.0002300
6	0	0	0.0425122	0	0	10	−0.0001028
7	0	0	−0.0205452	0	0	12	0.0000168
8	0	0	0.0055514	1	0	2	−0.0100233
0	2	0	0.4078091	2	0	2	0.0000840
0	3	0	−0.4359179	3	0	2	0.0018319
0	4	0	0.2871242	1	0	4	−0.0006666
0	5	0	−0.1552570	1	0	6	−0.0003195
0	6	0	0.0599375	2	0	4	0.0005178
1	1	0	−0.0116161	3	0	4	−0.0005862
2	1	0	0.0006295	0	1	2	−0.0355042
1	2	0	−0.0032075	0	1	4	0.0078318
2	2	0	−0.0057729	0	2	2	0.0120852
3	1	0	−0.0056214	0	2	4	0.0065616
1	3	0	0.0012072	0	3	2	−0.0043353
4	1	0	0.0030614	1	1	2	0.0014464
3	2	0	0.0054532	2	1	2	0.0033924
2	3	0	0.0040301	1	2	2	−0.0094339
1	4	0	−0.0009229	1	1	4	0.0045837

[a] See Eq. (1) for definition of PEF terms. Standard deviation of least-squares fit: 10^{-6} E_h

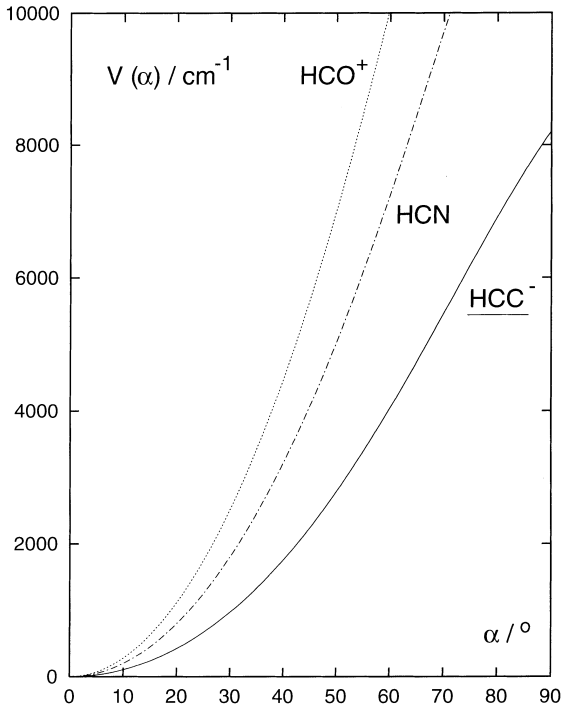

Fig. 1. Bending potentials for *HCC*$^-$, *HCN*, and *HCO*$^+$ [CCSD(T) results, see text]. The bond lengths are kept fixed at their equilibrium values

which involves only even powers of α, and

$$\mu^{\perp} = \sum_{ijk} D^{\perp}_{ijk} \Delta r^i \Delta R^j \alpha^k \quad , \tag{3}$$

in which k is an odd integer value. The coefficients $D^{\parallel}_{ijk}$ and $D^{\perp}_{ijk}$ are listed in Table 2. The present $D^{\parallel}_{ijk}$ coefficients referring to stretching vibrational coordinates are very similar to our previous values [13]. Among the $D^{\perp}_{ijk}$ coefficients, the linear term of the angular dependence is remarkably large. The corresponding coefficient for HCN [20] is smaller by a factor of 1.7.

Using the present CCSD(T) PEF (cf. Table 1) and electric dipole moment function (cf. Table 2), rovibrational term energies, wave functions and line intensities were calculated variationally. Watson's rovibrational Hamiltonian [23] was employed together with a basis set of harmonic oscillator – rigid rotor wave functions as first suggested and applied by Whitehead and Handy [24]. These calculations were carried out with a program written by one of us [8, 25]. They were restricted to low-lying vibrational states, but rotational excitation up to $J = 25$ was included. Results for the vibrational ground state and the first excited vibrational states are listed in Table 3. The excited states are well-separated from each other and undergo no substantial anharmonic interaction with other excited states; therefore conventional fits of the individual rovibrational transitions within one band are appropriate.

The spectroscopic constants G_v, B_v^{eff} and D_v^{eff} were obtained from least-squares fits to rovibrational energies with rotational quantum number up to $J = 25$, with separate fits being carried out in the e and f blocks. The G_v value for the first excited state of the bending vibration, (0 1^1 0), corresponds to the "rotationless" situation with $J' = 0$, for which the spectroscopic term "band center" is employed (see Ref. [26] for a thorough discussion). Although the HCC bending potential is rather shallow there is no pronounced anharmonicity effect on the first excited bending vibrational state. The ratio v_2/ω_2 amounts to 0.985 and is thus even slightly larger than the experimental value for HCN of 0.980 [27]. The band center of the v_2 band is predicted to be 511.1 cm^{-1}. According to our experience with HCN [20] and related

Table 2. CCSD(T) electric dipole moment function for HCC$^-$ [a]

i	j	k	$D^{\parallel}_{ijk}$	i	j	k	$D^{\perp}_{ijk}$
0	0	0	−1.26361	0	0	1	0.54292
1	0	0	0.12203	0	0	3	−0.17878
2	0	0	0.16301	0	0	5	0.11622
3	0	0	0.07615	0	0	7	−0.15601
4	0	0	0.03395	0	0	9	0.07540
5	0	0	−0.02498	1	0	1	−0.04741
0	1	0	0.65647	0	1	1	0.40473
0	2	0	−0.07893	1	1	1	0.02365
0	3	0	−0.04631	2	0	1	−0.04126
0	4	0	0.00758	0	2	1	−0.23236
0	0	2	0.40723	2	1	1	−0.20657
0	0	4	0.04201	1	2	1	0.07763
0	0	6	−0.11477	1	0	3	−0.01756
0	0	8	0.06412	0	1	3	−0.21622
1	1	0	0.09251	1	1	3	−0.09893
2	1	0	0.09894	1	0	5	0.02465
1	2	0	0.02758	0	1	5	0.02902
3	1	0	0.04379				
1	3	0	−0.05846				
2	2	0	−0.02788				
1	0	2	−0.02686				
0	1	2	−0.13251				
1	1	2	−0.04148				
2	0	2	−0.05567				
0	2	2	−0.07751				
1	0	4	−0.00837				
0	1	4	−0.00963				
1	1	4	0.23202				

[a] All coefficients are given in atomic units

Table 3. Spectroscopic properties for the ground state and the first excited vibrational states of HCC$^-$ [a]

Property	(0, 0^0, 0)	(0, 1^1, 0)	(0, 0^0, 1)	(1, 0^0, 0)
G_v (cm^{-1})	0	511.1	1805.0	3211.3
B_v^{eff} (MHz)	41568	41572, 41828 [b]	41261	41272
D_v^{eff} (kHz)	96.3	96.9, 101.6 [b]	96.4	95.6
μ_v (D)	−3.093 [c]	0.477 [d]	0.127 [d]	0.025 [d]
A_1^e		−0.00023	0.00294	−0.00826

[a] CCSD(T), all electrons correlated (basis: 250 CGTOs). Harmonic vibrational wavenumbers: $\omega_1 = 3355.4$ cm^{-1}, $\omega_2 = 518.7$ cm^{-1}; $\omega_3 = 1834.8$ cm^{-1}

[b] Rotational and centrifugal distortion constants for e and f blocks, respectively

[c] Permanent dipole moment

[d] Transition dipole moment

[e] First Herman-Wallis coefficient (see text)

molecules, this value may be in error by about $2\,cm^{-1}$. It lies well within the error bars of the approximate value of $505 \pm 20\,cm^{-1}$ deduced from the photoelectron spectrum [7]. Likewise, the calculated value of $1805.0\,cm^{-1}$ for the origin of the parallel band ν_3 agrees with the experimental value of $1800 \pm 20\,cm^{-1}$ [7]. The origin of the weak parallel band ν_1 (~CH stretch) is predicted at $3211.3\,cm^{-1}$, with an accuracy of about $2\,cm^{-1}$.

From the variational calculations, the differences $B_{0,0^0,0} - B_{1,0^0,0}$ and $B_{0,0^0,0} - B_{0,0^0,1}$ are obtained to be 296.8 and 307.5 MHz, respectively. They may be compared with the vibration-rotation coupling constants α_1 and α_3 as calculated by conventional second-order perturbation theory in normal-coordinate space. These are 293.8 and 304.8 MHz and thus smaller than the above values by only 1%. Likewise, the α_2 value of -133.4 MHz compares nicely with the corresponding value of -131.9 MHz obtained from the B_v^{eff} values of Table 3. The l-type doubling constant q_2 is 256.1 MHz (variational) and 247.8 MHz (perturbational). The difference $B_{0,0^0,0} - B_e$ is calculated to be -163.6 MHz (variational) and -165.9 MHz (perturbational), respectively. Using the former value together with the equilibrium rotational constant $B_e = 41\,800$ MHz obtained from the present corrected equilibrium structure we arrive at a $B_{0,0^0,0}$ prediction of 41 636(20) MHz, with a somewhat conservative error estimate given in parentheses.

The ground-state quartic centrifugal distortion constant is calculated to be 96.3 kHz and should be accurate to about 1%. It is larger than the corresponding experimental value for isoelectronic HCN [27] by 10%. As for HCN [27], vibrational excitation by one quantum leads to only minor changes in the D_v^{eff} values.

The ground-state dipole moment μ_0 of HCC^- is calculated to be -3.093 D. According to our experience with similar molecules, this value should be accurate to better than 0.01 D. The difference $\Delta\mu = \mu_0 - \mu_e$ amounts to 0.119 D which is four times larger than the corresponding value for HCN [20]. This rather big difference between HCC^- and HCN is mainly due to the shallow bending potential of HCC^-. Although the first microwave spectrum of a negative molecular ion was recorded only very recently, the large value of μ_0 and the high stability with respect to electron detachment should make HCC^- a promising candidate for forthcoming experimental studies by microwave spectroscopy.

From the rovibrational wave functions and the electric dipole moment function we have calculated the corresponding line intensities. Those of the P and R branches for all three fundamentals are mainly described by the two parameters μ_v (rotationless transition moment) and A_1 (first Herman-Wallis coefficient). They were derived from a fit to the squared effective transition moments via the formula

$$\left[\mu_v^{\text{eff}}(m)\right]^2 = (\mu_v)^2(1 + A_1 m + \cdots)^2 \qquad (4)$$

where the quantum number m has the value $-J''$ for P-branch transitions and $J'' + 1$ for R-branch transitions. The values $\left[\mu_v^{\text{eff}}(m)\right]^2$ were obtained from the squared transition moments R^2 of rovibrational transitions (see, for example, [28] for their definition) by division with the appropriate Hönl-London factors through which the major portion of the m dependence is removed. In agreement with our previous work [13], the ν_1 band is very weak and will thus be difficult to observe by IR absorption spectroscopy. In contrast to isoelectronic HCN, the A_1 value for this band is rather large and is negative. This has the consequence that lines in the P branch are stronger than the corresponding lines in the R branch. A stick spectrum of the ν_1 band at 273 K is given in Fig. 2, where the individual line intensities are normalized with respect to the strongest line within the P branch. The transition moment of the ν_3 band is calculated to be larger than that of the ν_1 band by a factor of 5.11, very close to our previous value of 4.96 [13]. The ν_3 band has a fairly small positive first Herman-Wallis coefficient and thus shows the usual relationship between the intensities of R- and P-branch lines. The perpendicular band ν_2 has a large transition moment of 0.477 D. It may thus be a suitable candidate for forthcoming experimental studies by high-resolution IR spectroscopy. The A_1 value for the P and R branches is calculated to be small. For the Q branch of the ν_2 band we calculate a very small Herman-Wallis coefficient of $A_2^Q = -1.12 \times 10^{-5}$ (see Ref. [29] for its definition). A stick spectrum of the whole ν_2 band at 273 K is given in Fig. 3, where the individual line intensities are normalized with respect to the strongest line within the Q branch.

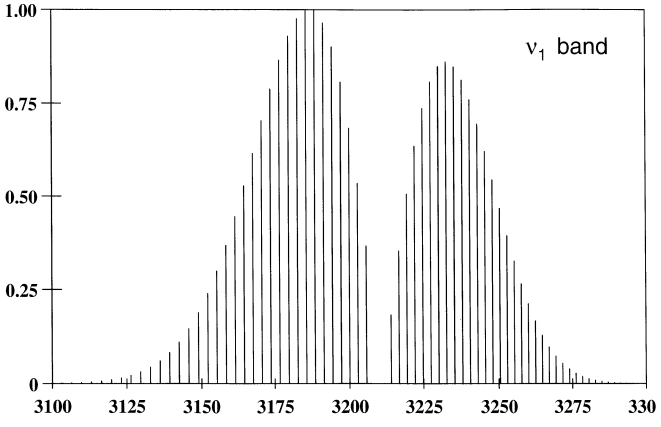

Fig. 2. Stick spectrum of the ν_1 band at 273 K

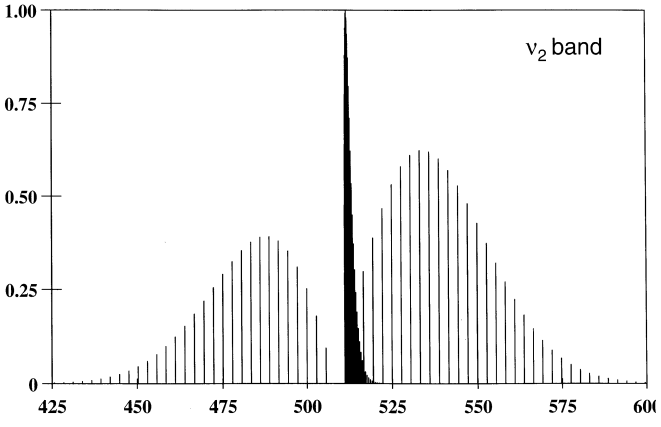

Fig. 3. Stick spectrum of the ν_2 band at 273 K

3 The energy barrier to isomerization

About 50 energy points were calculated in the vicinity of the barrier to isomerization and the locations of the two equivalent saddle points and the T-shaped local energy minimum between them were determined by suitable numerical techniques. Throughout, the large basis of 250 CGTOs was employed and all electrons were correlated in the post-Hartree-Fock calculations. Results are given in Table 4 where the corresponding values for the absolute linear energy minimum are also included for comparison. In accordance with our previous work [8, 9, 11, 12], all six methods employed (SCF, MP2, CCSD [30, 31], CCSD-T [32], CCSD(T), and CEPA–1) yield an "Eyring's lake" in the T-shaped configuration. The heights of the two equivalent saddle points with respect to this local energy minimum, $\Delta E(S-T)$, differ significantly, however. The CCSD-T and CCSD(T) results are very similar and should be accurate to at least $50\,\mathrm{cm}^{-1}$. MP2 overestimates $\Delta E(S-T)$ by more than a factor of 2. CEPA–1, which is considerably less expensive than CCSD-T or CCSD(T), does quite a good job and underestimates this quantity by roughly $100\,\mathrm{cm}^{-1}$.

4 Discrete variable representation (DVR)-distributed Gaussian basis (DGB) and finite basis representation (FBR) calculations with a CEPA–1 PES

Higher excited rovibrational states of HCC^- were investigated on the basis of the previous CEPA–1 PEF [8, 9]. It corresponds to a polynomial expansion

$$V - V_e^T = \sum_{ijk} C_{ijk} S_1^i S_2^j S_3^k \quad (j:\text{even}) \tag{5}$$

in symmetry coordinates $S_1,\ S_2,\ S_3$ referring to the local T-shaped energy minimum:

$$\begin{aligned} S_1 &= (r_1 + r_2 - 2r_e)/\sqrt{2} \\ S_2 &= (r_1 - r_2)/\sqrt{2} \\ S_3 &= R - R_e\ . \end{aligned} \tag{6}$$

r_1 and r_2 are the CH distances and thus in the above three equations S_1 and S_2 correspond to the symmetric and asymmetric CH stretching coordinates; S_3 is the CC stretching coordinate. The fit was based on 198 different CEPA–1 energy points up to about $25000\,\mathrm{cm}^{-1}$ above equilibrium and had a standard deviation of $1.7\,\mathrm{cm}^{-1}$ (see Table 5 for the coefficients C_{ijk}).

Table 5. Coefficients C_{ijk} (in a.u.) of the CEPA–1 PEF for HCC^-[a]

i	j	k	C_{ijk}	i	j	k	C_{ijk}
2	0	0	0.067503	3	0	2	−0.038292
3	0	0	−0.045160	4	0	2	0.007825
4	0	0	0.021063	1	2	1	0.021176
5	0	0	−0.011214	1	4	1	−0.012299
6	0	0	0.005256	2	2	1	−0.011902
7	0	0	−0.001437	2	4	1	0.007718
8	0	0	0.000202	3	2	1	0.008046
0	2	0	0.015695	3	4	1	−0.003962
0	4	0	0.017505	4	2	1	−0.006859
0	6	0	0.006446	4	4	1	0.002016
0	8	0	−0.000091	1	2	2	−0.013389
0	10	0	0.000005	1	2	0	−0.147103
0	0	2	0.357750	2	2	0	0.156595
0	0	3	−0.330587	3	2	0	−0.101873
0	0	4	0.211535	4	2	0	0.056151
0	0	5	−0.169370	5	2	0	−0.022303
0	0	6	0.040982	6	2	0	0.004983
0	2	1	0.031250	7	2	0	−0.000639
0	4	1	−0.002689	1	4	0	−0.035554
0	6	1	0.003870	2	4	0	0.043865
0	8	1	−0.000531	3	4	0	−0.035893
0	2	2	−0.056522	4	4	0	0.015296
0	4	2	0.006872	5	4	0	−0.003333
0	6	2	0.000792	6	4	0	0.000566
1	0	1	−0.032819	1	6	0	−0.011313
2	0	1	0.014293	2	6	0	0.008830
3	0	1	−0.010824	3	6	0	−0.003263
4	0	1	0.007361	4	6	0	0.000859
1	0	2	0.015626	5	6	0	−0.000246
2	0	2	0.053130				

[a] For the geometrical parameters and the relative energy of the local T-shaped energy minimum see Table 4. See Eq. (5) for definition of coordinates

Table 4. Geometrical parameters and relative energies of stationary points on the potential hypersurface for H migration in HCC^-[a]

Stationary point		SCF[b]	MP2[b]	CEPA-1[b]	CCSD[b]	CCSD-T[b]	CCSD(T)[b]	CEPA−1[c] [8]
L	r_e (CH)	1.0572	1.0675	1.0676	1.0664	1.0696	1.0697	1.0705
	R_e(CC)	1.2229	1.2486	1.2421	1.2393	1.2470	1.2474	1.2493
	E_{rel}	0	0	0	0	0	0	0
T	r_e(H-M)[d]	1.0859	1.0699	1.0818	1.0792	1.0820	1.0821	1.0873
	R_e(CC)	1.2593	1.2808	1.2759	1.2736	1.2807	1.2810	1.2845
	E_{rel}	7460	8219	7704	7747	7800	7818	7591
S	r_s(H-M)[d]	1.1950	1.1971	1.1651	1.1815	1.1808	1.1795	1.1704
	R_s(CC)	1.2604	1.2734	1.2754	1.2719	1.2783	1.2788	1.2838
	α_s	19.80	20.42	16.26	18.37	17.91	17.76	16.25
	$\Delta E(S\text{-}T)$	445	872	283	423	401	391	271

[a] Bond lengths in Å and relative energies in cm^{-1}. The angle α_s (in degrees) measures the deviation from the T form. L stands for the linear global minimum, T for the T-shaped configuration, and S for the saddle point
[b] Basis 250 CGTOs, all electrons correlated in post-Hartree-Fock calculations
[c] Valence electrons correlated
[d] Distance between proton and center of the CC unit

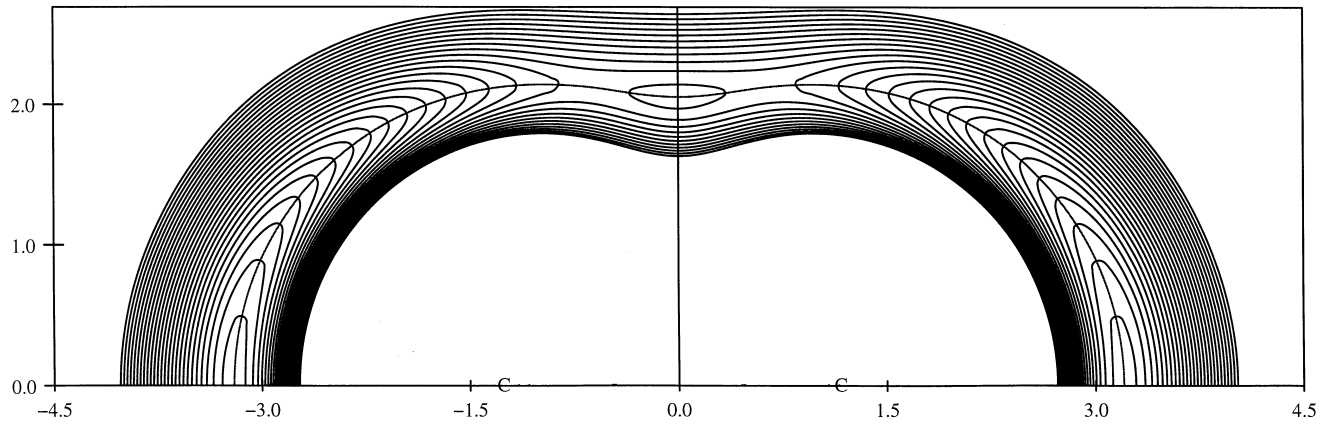

Fig. 4. Migration of the proton around the CC subunit for the CEPA–1 potential energy function. The rectangular coordinates (in a.u.) describe the position of the proton in a coordinate system with origin at the center of the CC bond and abscissa identical to the CC bond axis. The energy is minimized with respect to the CC distance. Contour lines are drawn at intervals of $500\,cm^{-1}$ with the first contour placed $250\,cm^{-1}$ above linear equilibrium. The minimum energy path (MEP) is designated by a *solid line*

As is obvious from Table 4, the previous CEPA–1 PEF reproduces the geometric and energetic positions of the stationary points quite well in comparison to the more accurate CCSD(T) results. The band centers of the fundamentals of HCC^- are calculated to be $3216.7\,cm^{-1}$ (ν_1), $509.7\,cm^{-1}$ (ν_2), and $1814.9\,cm^{-1}$ (ν_3). They agree with our previous values [8, 9, 13]; note that the R(0) line position (at $512.5\,cm^{-1}$) was quoted as "ν_2^1" in that work. The CEPA–1 values differ from the present CCSD(T) results by only $5.4\,cm^{-1}$ (ν_1), $-1.4\,cm^{-1}$ (ν_2), and $9.8\,cm^{-1}$ (ν_3). The migration of the proton around the CC subunit on the CEPA–1 PEF is displayed graphically in Fig. 4. Throughout, the CC distance is optimized and the minimum energy path (MEP) is indicated by a full line.

In the calculation of rovibrational states we employed the vibration-rotation Hamiltonian for triatomic molecules in the body-fixed reference frame and Jacobi coordinates R, r and θ [33]. Here, R is the CC bond length, r the distance between the proton and the center of mass of CC, and θ the angle enclosed by the two radial vectors. A discrete variable representation (DVR) for the angular variable θ and a real 2D distributed Gaussian basis (DGB) for the radial coordinates are used in the DVR-DGB approach. The interested reader is referred to an earlier paper [34] for technical details. Initially, we also carried out calculations using both internal and Jacobi coordinates with a finite basis representation (FBR) method which is described elsewhere [35] and which led to numerically identical results.

The level assignments were made by combining an analysis of dominant zero-order components with inspection of expectation values of Jacobi coordinates. The separability of the (R, r, θ) motions is studied by reexpanding the exact wave functions into adiabatic subspaces obtained in the adiabatic stretch-bend approximation. This procedure is easy to implement within the DVR-DGB scheme because effective, adiabatic bending potentials are readily given by the two-mode stretching eigenenergies calculated as a function of the Jacobi angle (i.e., at chosen DVR angles). As proposed by Bačić and Light [36, 37], the adiabatic energies and corresponding adiabatic eigenvectors can be calculated by diagonalizing adiabatically rearranged Hamiltonian matrices. Our adiabatic projection assignment scheme makes use of a DVR-ray eigenvector basis [34] and is therefore different from the approach of Bačić [37] based on a DVR-adiabatic-vibrational-eigenstate basis. Our method also extends to the $J \neq 0$ situation. In our earlier studies it proved valuable in understanding the rovibrational energy structure of the HN_2^+ [38] and HCO^+/HOC^+ [39] systems. For selected J and k, where k is the quantum number of the projection of the total angular momentum J on the body-fixed z-axis, the adiabatic eigenfunctions $|v_1 v_2^k v_3\rangle$ of the well-defined quantum numbers v_1, v_2, k, and v_3 are calculated and subsequently used to obtain the adiabatic expansions of the exact wave functions. The assignment, whenever meaningful, is made by identifying the leading coefficient in these wave function expansions.

The potential profile along the minimum energy path (MEP) and the first nine adiabatic bending profiles are shown in Fig. 5. The barrier heights along the individual adiabatic profiles change prominently with (v_1, v_3) excitation. That of the ground state is $7322\,cm^{-1}$ and thus lower than the bare potential barrier height by $540\,cm^{-1}$. Single excitation of the stretching vibrations leads to further lowering by $77\,cm^{-1}$ for (0, 1) and $935\,cm^{-1}$ for (1, 0), respectively. This is best understood by examining the variation of the stretching frequencies along the MEP (see Fig. 6). The adiabatic CH stretching frequency ω_1^{adi} decreases from $3233\,cm^{-1}$ at linear geometry to $2280\,cm^{-1}$ at the saddle point and is rather constant over the region of the T-shaped local minimum. The adiabatic CC frequency drops from $1821\,cm^{-1}$ at the linear geometry to its minimum value of $1737\,cm^{-1}$ at $\theta = 55°$ and then increases to $1749\,cm^{-1}$ at $\theta = 90°$.

In this work assignments based on a 2D oscillator and on a 2D rotor model are used for the bending vibration. In the 2D oscillator model, the vibrational angular momentum l can have $v_2 + 1$ values $-v_2$, $-v_2 + 2, \ldots, v_2 - 2, v_2$ for a given v_2. The double-well symmetry of HCC^- is indicated by $+$ or $-$ exponents for levels which are symmetric or antisymmetric with respect to permutation of the C atoms. The highly

excited bending levels can alternatively be assigned according to the 2D rotor model in which l can assume $2v_2+1$ values $-v_2, -v_2+1, \ldots, v_2-1, v_2$ for a given v_2. In a body-fixed reference frame $l=k$. To illustrate the assignment scheme adopted for the bending vibration, k-block eigenenergies ${}^{(2)}E^k$ for $k=0,1,2$ calculated by neglecting the vibration-rotation interaction (the rotational energy is included) and the exact $E^{J,p}$ rovibrational energies calculated for $J=2$ in both parities are shown in Fig. 7. Only the bending progression associated with the ground state $(v_1=0, v_3=0)$ of the stretches is displayed. The k-block eigenstates clearly show two different patterns for energies below the ground-state adiabatic barrier $V_{\mathrm{bar}}^{(0,0)}$ (see Fig.5) at 9908 cm^{-1} and above 10 500 cm^{-1}, typical for the 2D oscillator and the 2D rotor model, respectively. The k-block eigenstates are used as zero-order components in our analysis of the more complicated structure of the exact rovibrational levels which is reported in Sect. 4.2.

We studied the vibrational states up to 20 000 cm^{-1} above the linear global minima. As there are 602 $J=0$ eigenstates in this energy range, we report here only selected energy levels in order to demonstrate character-

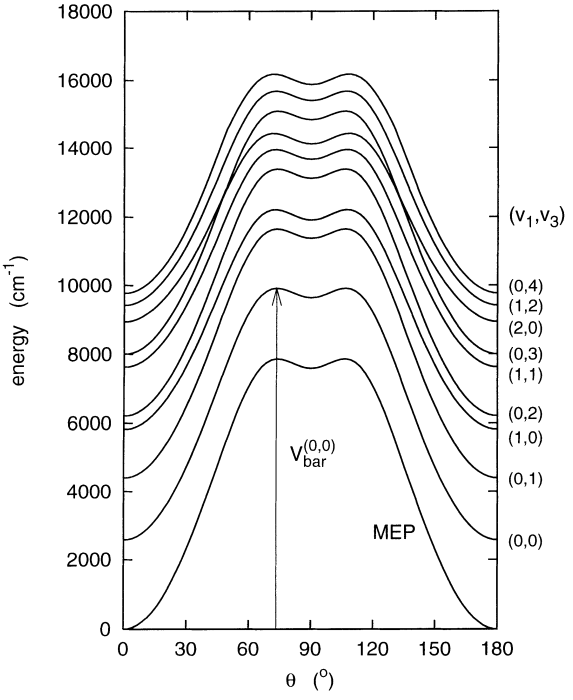

Fig. 5. MEP (*lowest curve*) and first nine adiabatic profiles for HCC^- as a function of the Jacobi angle θ

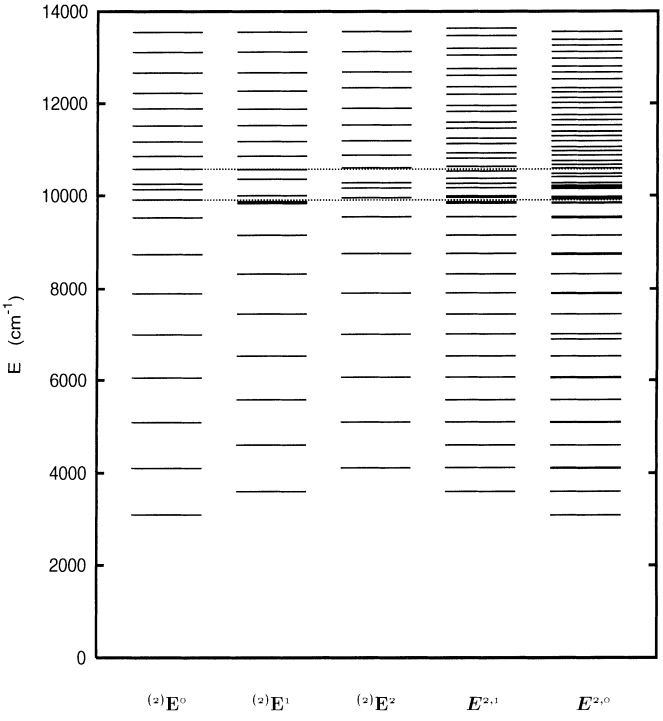

Fig. 7. Comparison of the k-block eigenvalues ${}^{(2)}E^k$ for $k=0$, 1, and 2, calculated by neglecting the vibration-rotation coupling, with the exact rovibrational energies $E^{2,p}$ for $J=2$. Only pure bending levels are shown. The *dotted lines* at 9908 and 10 500 cm^{-1} show the position of the ground-state adiabatic barrier and the energy where the onset of rotor-like structure takes place

Fig. 6a,b. Variation of the adiabatic stretching wavenumbers with the Jacobi angle θ. **a** CH stretching wavenumbers ω_1^{adi}. **b** CC stretching wavenumbers ω_3^{adi}

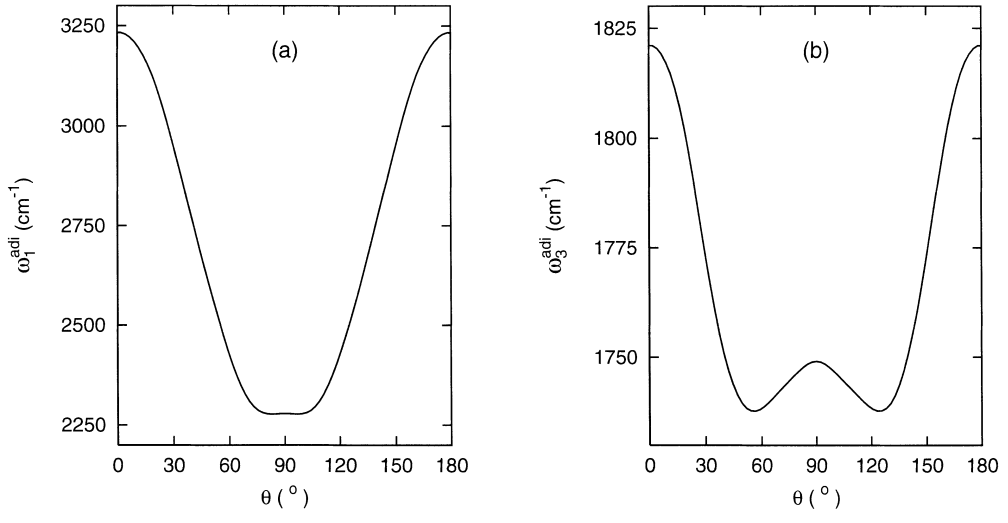

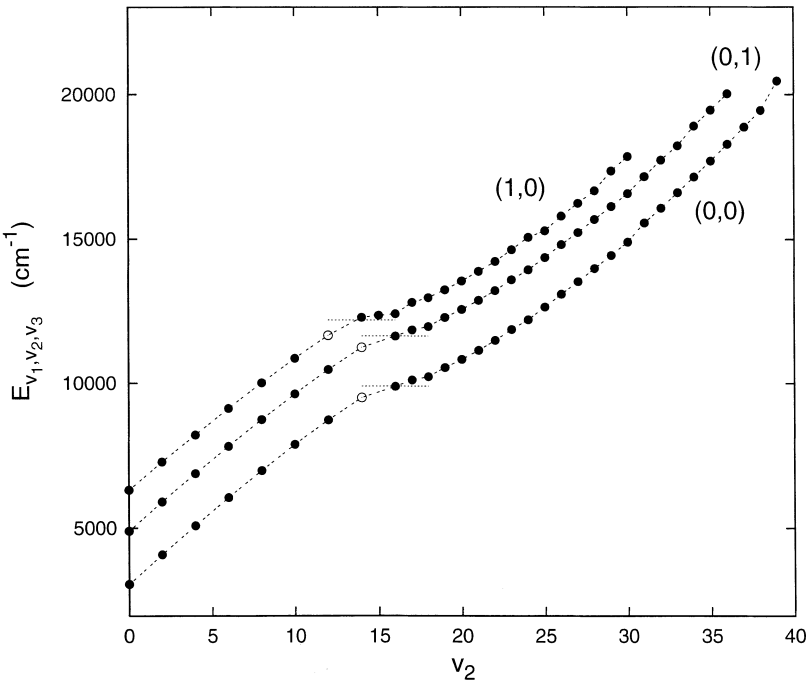

Fig. 8. Variation of the level energy with the v_2 level assignment for three (v_1, v_3) stretching excitations: (0, 0), (0, 1), and (1, 0). The *dotted lines* show the positions of the corresponding adiabatic barriers. The tunneling pairs are given by *empty circles*

istic energy patterns and trends in different energy regions.[1] In the following, the levels are frequently designated by their ordinal number $n^{J,p}$ for a given total angular momentum J and parity p.

The primitive 2D Gaussian functions were distributed at 23 000 cm^{-1} following closely the procedure described in Ref. [34]. The rovibrational levels of HCC^- were calculated employing 75 DVR points and a 2D-ray energy cutoff at 30 000 cm^{-1}.

4.1 Vibrational ($J = 0$) structure

The bending level energies of HCC^- for three different stretching excitations and $J = 0$ are shown in Fig. 8 as a function of the v_2 level assignment. The levels below and above the adiabatic barriers $V_{\text{bar}}^{(v_1,v_3)}$ are assigned employing the 2D oscillator and the 2D rotor model, respectively. All of the former levels are essentially doubly degenerate. Only states with energies close to $V_{\text{bar}}^{(v_1,v_3)}$ show noticeable tunneling splitting, as indicated by the empty circles in Fig. 8. The tunneling pairs shown are (0 14^0 0), (0 14^0 1), and (1 12^0 0). Their energy splittings are calculated to be 1.69, 1.89, and 1.36 cm^{-1}, respectively.

Two groups of vibrational states can clearly be identified in Fig. 8. In the lower energy regime, the level energies depend almost linearly on the quantum number v_2 label as in a harmonic oscillator, but they develop the pattern of a rotor with a quadratic dependence on v_2 in the high-energy regime. The transition between these two patterns closely coincides with the effective barrier positions. This is in good agreement with previous studies of triatomic molecules [34, 36, 38, 39], where it was shown that the onset of delocalization is determined by the effective adiabatic potential. It is worth emphasizing that the influence of the bend anharmonicity cannot be seen on the energy scale of Fig. 8. The dominant anharmonic mixing is of the type $\Delta v_2 = \pm 2$. It increases with v_2 excitation and is particularly important in the vicinity of the adiabatic barrier.

In Fig. 9 we show the variation of the expectation value $\sqrt{\langle\theta^2\rangle}$ of the Jacobi angle with level energy for $J = 0$, where $\sqrt{\langle\theta^2\rangle}$ is defined by

$$\sqrt{\langle\theta^2\rangle} = \cos^{-1}(\sqrt{\langle\cos^2\theta\rangle}) \ . \tag{7}$$

The levels with the same bending (and different stretching) excitation are connected by a line in Fig. 9: the first line displays $(v_1, v_2 = 0, v_3)$ levels, the second $(v_1, v_2 = 2, v_3)$, the third $(v_1, v_2 = 4, v_3)$, etc., with associated $\sqrt{\langle\theta^2\rangle}$ values of $\sim 10°$, 17°, 22°, etc., respectively. The vast majority of the $\sqrt{\langle\theta^2\rangle}$ values displays rather high insensitivity to the stretching excitation for $v_2 \leq 14$, such that $\sqrt{\langle\theta^2\rangle}$ provides a particularly good guide for assignments of levels with different v_2 excitations. The irregularities, like those seen for $v_2 = 8$ and 12 at $\sim$10 500 and 12 200 cm^{-1} in Fig. 9, reflect an important mixing of various zero-order components. The adiabatic projection assignment scheme has shown that mixing of the components $|0\ 8^0\ 2\rangle$ and $|0\ 12^0\ 1\rangle$ takes place at an energy of about 10 500 cm^{-1} and mixing of $|0\ 8^0\ 3\rangle$ and $|0\ 12^0\ 2\rangle$ occurs at about 12 200 cm^{-1}. The wave functions of the levels with $(v_1 = 0,\ v_2 < 14)$ and $(v_2 < 12,\ v_3 = 0)$ are fully localized in the region of the absolute linear minima. One should note the presence of high-lying localized states (asociated even with very small values of $\sqrt{\langle\theta^2\rangle}$) in which excitation primarily resides in the stretching modes. For making quick

[1] The complete list of calculated energy levels is available upon request from one of us (mmladen@gwdg.de)

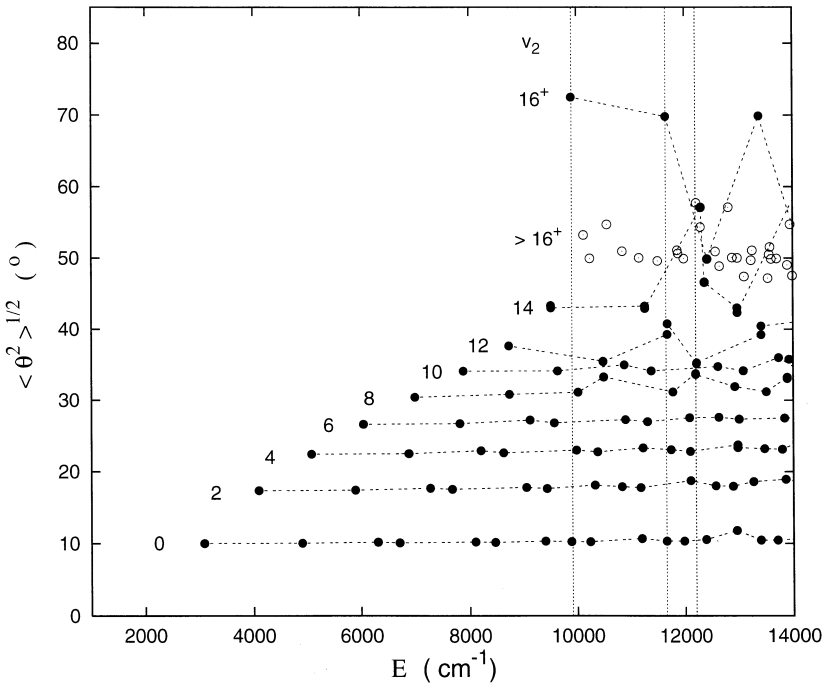

Fig. 9. Expectation value of the Jacobi angle θ as a function of level energy. The positions of the (0, 0), (0, 1), and (1, 0) adiabatic barriers are indicated by vertical *dotted lines*. The *empty circles* show the states with more than 16 quanta in the bending mode

preliminary quantum number assignments to calculated states the expectation values of the Jacobi coordinates were of great assistance for both the DVR- and FBR-based methods employed in this work. An automatic assignment scheme based solely on expectation geometries was previously employed by Bowman et al. [40].

The vibrational levels assigned as $(0\ 16^{0,+}\ 0)$, $(0\ 16^{0,+}\ 1)$, and $(0\ 16^{0,+}\ 2)$ exhibit very high $\sqrt{\langle\theta^2\rangle}$ values of about 70° in Fig. 9. These states lying at 9901 cm^{-1}, 11 647.6 cm^{-1}, and 13 378.5 cm^{-1} are only a few wavenumbers below the corresponding adiabatic barriers at 9908 cm^{-1} ($V_{bar}^{(0,0)}$), 11 652 cm^{-1} ($V_{bar}^{(0,1)}$), and 13 380 cm^{-1} ($V_{bar}^{(0,2)}$). In order to quantify localization of a wave function ψ_α in the region of the T-shaped well, defined by $\theta \in (75°, 105°)$, we introduce the integrated wave function amplitude P_T as

$$P_T = \int_{75°}^{105°} d\theta \int |\psi_\alpha|^2 \, d\Omega \tag{8}$$

where Ω stands for the two radial coordinates R, r, and the three Euler angles. The quantity P_T has very large values of 72%, 67%, and 67% for the vibrational levels $(0\ 16^{0,+}\ 0)$, $(0\ 16^{0,+}\ 1)$, and $(0\ 16^{0,+}\ 2)$, indicating significant localization of the corresponding wave functions in the region of the T-shaped local minimum. In Fig. 9, the third level with $v_2 = 14$ (at 12 299.2 cm^{-1}) and the third level with $v_2 = 16$ (at 12 420.6 cm^{-1}) correspond to the states $(1\ 14^{0,+}\ 0)$ and $(1\ 16^{0,+}\ 0)$ with the CH stretching mode excited by one quantum. Both states are located above the corresponding adiabatic barrier at 12 205 cm^{-1} (Fig. 8) and exhibit a smaller localization in the T-shaped well, as seen by the P_T values which are calculated to be only 33% and 23%.

The majority of the states with $v_2 > 16^+$, which are marked by empty circles in Fig. 9, exhibit the expectation values $\sqrt{\langle\theta^2\rangle}$ clustered around 50°. The corresponding P_T values are calculated to be 12–19%, compared with P_T of 17% (= 100%/6) for a wave function uniformly distributed over the entire angular region. In Fig. 8, these levels were classified as rotor-like states. The effective rotational constant for free rotor states is given by

$$f(R,r) = \frac{1}{2\mu_R R^2} + \frac{1}{2\mu_r r^2} \ , \tag{9}$$

where $\mu_R = m_C/2$ and $\mu_r = 2m_H m_C/(m_H + 2m_C)$ for HCC^-; the quantity $2f(R,r)$ represents the reduced mass attributed to the Jacobi angle [33]. The expectation values $\langle f \rangle$ of the effective rotational constant calculated for the rotor-like states ($v_2 > 16$) are shown in Fig. 10. Comparison to f_{adi} and f_{diff} is also given, where f_{adi} and f_{diff} are calculated from the energy differences between the adjacent energy levels v_2,

$$E^{adi}(0, v_2^0, 0) - E^{adi}[0, (v_2 - 1)^0, 0] = 2\, f_{adi}\ v_2 \tag{10}$$

$$E^{0,0}_{0,v_2^0,0} - E^{0,0}_{0,(v_2-1)^0,0} = 2\, f_{diff}\ v_2 \ , \tag{11}$$

by assuming the validity of the rotor term formula $v_2(v_2 + 1)$ at these energies. The adiabatic energies $E^{adi}(v_1, v_2^k, v_3)$ are calculated by neglecting the stretch-bend coupling (used in Eq. (10)). The exact vibrational energies $E^{J,p}_{v_1,v_2^l,v_3}$ are employed to calculate f_{diff} in Eq. (11).

The smooth curve representing f_{adi} as a function of the level v_2 assignment asymptotically approaches a limiting value of 10.2 cm^{-1} for $v_2 > 30$. The more complicated structures of $\langle f \rangle$ and f_{diff} in Fig. 10 are due to the effects of mode mixing occuring in treatments beyond 1D. For instance, an abrupt increase in $\langle f \rangle$ or decrease in f_{diff} at $v_2 = 24$ in Fig. 10 is the consequence

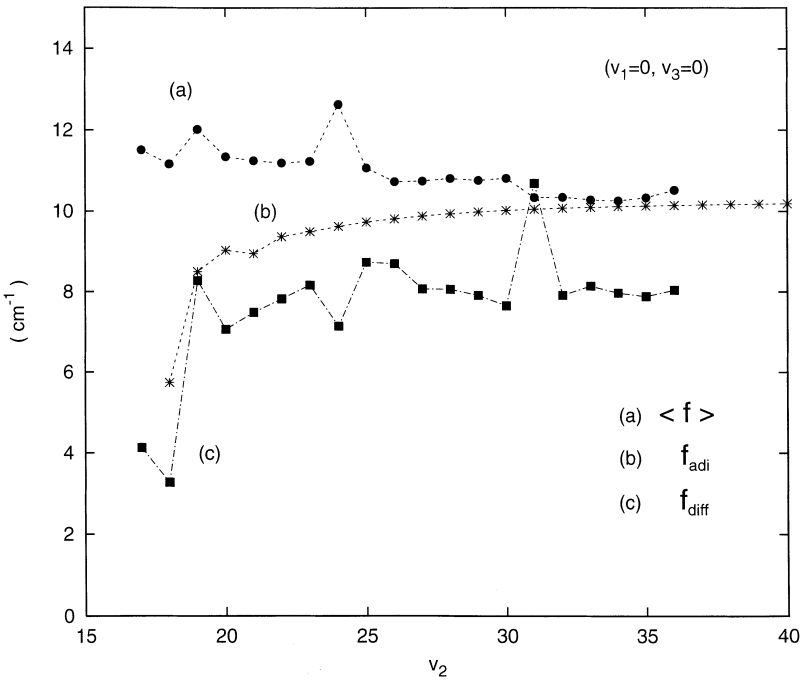

Fig. 10. Effective rotational constants calculated for the rotor-like states ($J = 0$) and ground-state stretching vibrations. For additional explanations, see text

of a resonance interaction which couples the adiabatic states $|0\ 24^{+}\ 0\rangle$ and $|1\ 14^{+}\ 0\rangle$ in the following manner:

$$|n^{0,0} = 117\rangle \sim 0.650\ |0\ 24^{0,+}\ 0\rangle - 0.656\ |1\ 14^{0,+}\ 0\rangle$$
$$|n^{0,0} = 121\rangle \sim 0.535\ |0\ 24^{0,+}\ 0\rangle + 0.668\ |1\ 14^{0,+}\ 0\rangle\ , \tag{12}$$

using 2D-oscillator notation. These two-component descriptions provide 85% and 73% of the exact vibrational levels $n^{0,0} = 117$ and 121 lying at 12 216.5 cm^{-1} and 12 299.2 cm^{-1}, respectively. A similar effect is also found for the state with $v_2 = 30$ which exhibits very extensive mixing with $(1\ 24^{0,+}\ 0)$. The states of a resonant pair exhibit extremely similar expectation geometries.

4.2 Rotation and Coriolis resonances

The rovibrational levels of HCC^{-} were calculated for $J = 0, 1$, and 2 in both parities and the energy levels up to the fourth adiabatic barrier $V_{bar}^{(1,1)}$ at 13952 cm^{-1} were investigated in particular detail. Two groups of rovibrational levels are identified, which can be classified as groups of k-assignable and of k-nonassignable states. This division of states was made by calculating the probability ${}^{(J,p)}P_k$ for each exact eigenfunction ψ_α, where

$${}^{(J,p)}P_k = |\langle\psi_\alpha|Jpk\rangle|^2\ , \tag{13}$$

which offers a measure of the goodness of the k quantum number. For a given J, the possible k values are $k \leq J$.

The projection of the total angular momentum J on the body-fixed z-axis is assigned a good quantum number k if there is a single, dominant probability ${}^{(J,p)}P_k$ for a given J and p. This is the case for all energy levels $(v_1\ v_2^l\ v_3)$ lying below the corresponding adiabatic barrier $V_{bar}^{(v_1,v_3)}$. The expectation geometries of the k-assignable states are rather insensitive to rotational excitation. Furthermore, these levels are not distinctively affected by Coriolis interaction, as seen in Fig. 7 for $J = 2$ where $E^{2,p} \sim^{(2)} E^k$ at energies below 9908 cm^{-1}.

Rotational excitation decreases the tunneling splitting for $v_1 = 0$, but increases it when $v_1 = 1$. For $J = 1$, an energy splitting of 1.45 and 1.80 cm^{-1} is calculated for $(0\ 14^0\ 0)$ and $(0\ 14^0\ 1)$, compared with the corresponding $J = 0$ values of 1.69 and 1.89 cm^{-1}. For the excited CH stretching mode the tunneling splitting of the $(1\ 12^0\ 0)$ pair is calculated to be 1.36 cm^{-1} for $J = 0$ and 1.81 cm^{-1} for $J = 1$. The first $k = 1$ tunneling pair $(0\ 15^1\ 0)$ has an energy splitting of 36.7 cm^{-1} in odd parity and a splitting of 28.8 cm^{-1} in even parity. The $k = 2$ tunneling pair $(0\ 14^2\ 0)$ is split by 1.1 cm^{-1}, which is smaller than in the corresponding $k = 0$ pair.

At energies above 10 500 cm^{-1} the exact rovibrational levels of HCC^{-} in Fig. 7 reveal complicated patterns due to Coriolis resonance interactions. All levels here are strongly coupled and an unambiguous k-assignment is no longer possible due to very prominent mixing, which results in almost equal probabilities ${}^{(J,p)}P_k$ for interacting k-subspaces. The exact levels involed in Coriolis resonances exhibit similar expectation geometries.

The Hamiltonian term [34] which gives rise to c-axis Coriolis resonances is proportional to $\{i\hbar\hat{L}_y\frac{\partial}{\partial\theta} + \cot\theta\ \hat{L}_x\hat{L}_z\}$. It leads to particularly strong coupling of $(k, k \pm 1)$-type when the zero-order components in adjacent k-blocks are nearly degenerate. This is the case for the ${}^{(2)}E^k$ levels of HCC^{-} lying above 10 500 cm^{-1} in Fig. 7. In order to avoid any ambiguity regarding the orientation of the body-fixed reference frame, the rovibrational levels of HCC^{-} for $J = 1$ in odd parity were calculated by aligning the z-axis either with the CC bond vector or with the Jacobi vector. These two situations are formally described by the same kinetic

energy operator [41]. The present DVR-DGB approach has additionally been adapted to the body-fixed reference frame which follows principal axes of the moment-of-inertia tensor, for which the rotational contribution is as in Ref. [42]. These three selections for the quantization of the overall angular momentum led to the same conclusions concerning the presence of Coriolis resonances in the rovibrational energy spectra of the acetylide anion.

Levels of different symmetry are particularly strongly mixed by the Coriolis interaction [43, 44]. For the purpose of illustration, Fig. 11 shows Coriolis resonances $n^{1,1} = 197{,}201$ lying at 11805.1 and 11937.7 cm^{-1} for $J = 1$ in odd parity. These resonances originate from a pair of $k = 0$ and $k = 1$ levels assigned as $(0\ 22^{0,-}\ 0)$ and $(0\ 23^{1,+}\ 0)$ in the 2D oscillator model or, alternatively, as $(0\ 23^{0}\ 0)$ and $(0\ 23^{1}\ 0)$ in the 2D rotor model. The $k = 0$ zero-order component, calculated by neglecting vibrational-rotation coupling, differs form the $J = 0$ level at 11873.5 cm^{-1} (the state $n^{0,0} = 105$ in Fig. 11) only in the rotational ($J = 1$) energy. The $k = 1$ zero-order component coincides perfectly with the $J = 1$ (even parity) state $n^{1,0} = 95$ at 11 871.4 cm^{-1}. The wave functions for $n^{0,0} = 105$ and $n^{1,0} = 95$ in Fig. 11 have different numbers of nodes and different symmetry. The former wave function has 23 and the latter one 22 nodes along the bending coordinate. The resonances $n^{1,1} = 197{,}201$ exhibit no exchange symmetry, as evidenced by different number of nodes N_1 and N_2 in the two θ intervals: $(0°, 90°)$ and $(90°, 180°)$, respectively. While the wave function of $n^{1,1} = 197$ has N_1 and N_2 of 11 and 12, for the wave function of $n^{1,1} = 201$ the situation is reversed with N_1 and N_2 of 12 and 11. Symmetry breaking as observed in Fig. 11 for $n^{1,1} = 197{,}201$ has been encountered in all cases where Coriolis coupling plays an important role. Extensive mixing of the $k = 0$ and $k = 1$ subspaces for the pair $n^{1,1} = 197{,}201$ is additionally evident in the quantity $^{(1,1)}P_k$, which is 0.5 for both $k = 0$ and 1.

A comment should be made regarding the assignments of the states shown in Fig. 11. The level $n^{0,0} = 105$ was actually difficult to assign because this state is involved in the resonance interaction as follows

$$\begin{aligned} |n^{0,0} = 104\rangle &\sim 0.643\ |0\ 16^{0,-}1\rangle\ -\ 0.609\,|0\ 22^{0,-}\ 0\rangle \\ |n^{0,0} = 105\rangle &\sim 0.625\ |0\ 16^{0,-}1\rangle + 0.633\,|0\ 22^{0,-}\ 0\rangle \end{aligned} \tag{14}$$

when the 2D oscillator model is applied. In order to arrive at a more complete understanding of the level origin (as well as of the barrier region), the following test was performed. The PEF was modified such that the T-shaped well is suppressed. This was achieved by setting the potential energy to the constant value $V(R, r, 75^o)$ over the region $\theta \in (75^o,\ 105^o)$. This modification does not influence the absolute minima at linear geometry or the barrier height. The interaction suppressed by this modification appeared to be crucial for coupling between bending levels corresponding to neighbouring $(0,v_3)$ adiabatic profiles. The resonance pair in Eq. (14) was easy to assign on the modified PES, leading to our suggestion that the level $n^{0,0} = 105$ originates from $(0\ 22^{0,-}\ 0)$.

Coriolis-type interaction can prominently affect the mixing of the zero-order components. An example of this is rotational excitation of the anharmonic resonances $n^{0,0} = 104,\ 105$ from Eq. (14), which is shown schematically in Fig. 12. An important consequence of the pronounced off-diagonal Coriolis $(k, k \pm 1)$ coupling,

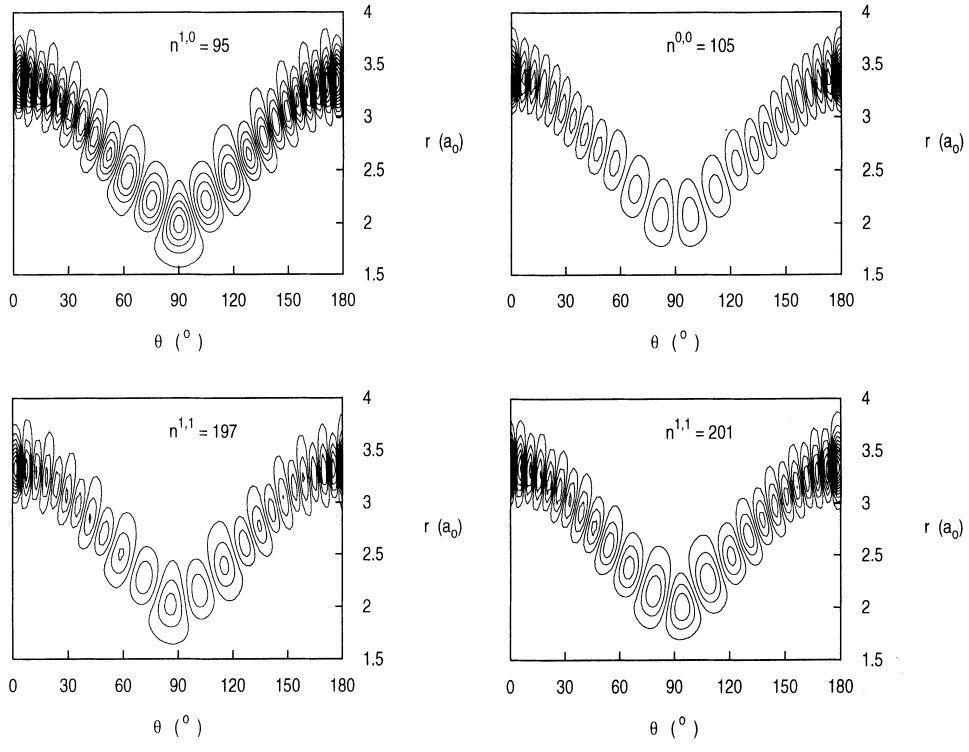

Fig. 11. 2D contour plots of wave functions integrated over the Euler angles for the levels $n^{0,0} = 105$ and $n^{1,0} = 95$ that are involved in Coriolis resonance $n^{1,1} = 197{,}201$ for J = 1 (odd parity). The CC distance is fixed at its expectation value

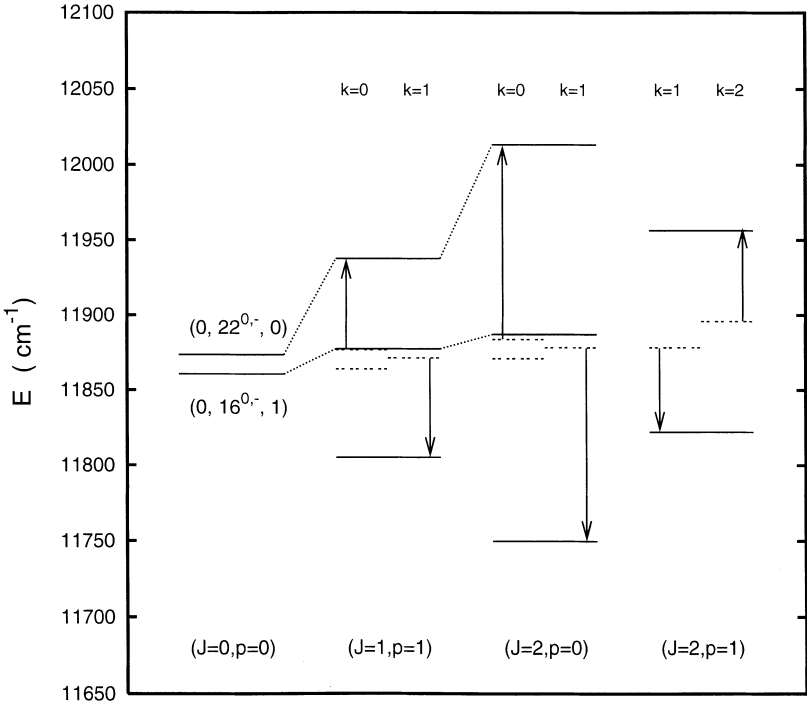

Fig. 12. Rotational excitation of the anharmonic resonances $n^{0,0} = 104,105$. The *dashed lines* represent k-block eigenenergies ${}^{(J)}E^k$ calculated by neglecting the vibration-rotation interaction. The *arrow* connects the zero-order component ${}^{(J)}E^k$ with the exact rovibrational level $E^{J,p}$ originating from ${}^{(J)}\mathrm{E}^k$

involving only the vibrational level $(0\ 22^{0,-}\ 0)$ in Fig. 12, is a weaker mixing of the adiabatic states in Eq. (14), such that the level $(0\ 16^{0,-}\ 1)$ is unambiguously assigned for $J \neq 0$. The Coriolis resonances are split by 133 and 263 cm^{-1} for $J = 1$ (odd parity) and 2 (even parity), respectively. The Coriolis resonances involving the levels $(0\ 23^{1,+}\ 0)$ and $(0\ 22^{2,-}\ 0)$ for $J = 2$ in odd parity exhibit a splitting of 134 cm^{-1}.

The dashed lines in Fig.12 show the k-block eigenenergies ${}^{(J)}E^k$ calculated by switching off the Coriolis term in the kinetic energy operator. One should note that in Fig.12 the relative positions of the ${}^{(J)}E^k$ states in different k-blocks coincide with the relative positions of the exact rovibrational levels calculated by switching on the Coriolis term. Therefore, inspection of the ${}^{(J)}E^k$ levels is very instructive for predicting whether the exact level is perturbed from "below" or from "above" and for making quick preliminary k assignments to exact rovibrational levels. The presence of strong Coriolis resonances, like those discussed in this work for HCC^-, can be used as a safe criterion for identifing rotor-like states of any triatomic molecule.

5 Conclusions

Coupled-cluster calculations with a large basis set of 250 GTOs were carried out with the aim to predict the ground-state rotational constant with about 20 MHz accuracy and the wavenumbers of the fundamental vibrational transitions with an accuracy of a few reciprocal centimeters. The large ground-state dipole moment μ_0 of -3.093 D and the high stability with respect to electron detachment should make HCC^- a promising candidate for forthcoming experimental investigation by microwave spectroscopy. A large transition dipole moment of 0.477 D is calculated for the HCC bending vibration with band center at 511.1 cm^{-1}. The first Herman-Wallis coefficient for the weak ν_1 band is fairly large with the consequence that lines in the P branch are stronger than the corresponding lines of the R branch.

All methods of electronic structure theory employed yield a shallow local energy minimum in a T-shaped configuration. CCSD(T) and CCSD-T calculations yield barrier heights for the two equivalent saddle points of 391 and 401 cm^{-1}, respectively.

An extensive study has been devoted to the understanding of the main vibrational interactions of HCC^- on the previous CEPA–1 PEF [8, 9]. The zero-order character of eigenstates is analyzed employing an adiabatic projection scheme, which is well-suited for automatic state assignments as well as for understanding the importance of the mode-mode couplings. Even though mixing of the HCC bending and the CH stretching modes dominates the vibrational structure of HCC^-, several instances of resonance mixing between states of different ν_3 (CC stretch) excitations are found. The appearance of rotor-like characteristics in the vicinity of an adiabatic barrier is clearly shown for bending levels with identical stretching excitation. For HCC^-, the vibrational levels with $\nu_2 > 16^+$ exhibit this rotor-like behavior related to rotation of the proton around the CC bond.

Coupling between the rotational and vibrational degrees of freedom participates prominently in the overall molecular behaviour of HCC^- and leads to complicated energy patterns with particularly strong Coriolis resonances at energies where the k-block eigenstates display the onset of the rotor-like structure. Anharmonic resonances are most sensitively dependent on rotational excitation.

Acknowledgements. M.M. and S.C. express their gratitude to the Deutsche Forschungsgemeinschaft for financial support (through Grant No. Ml 7/1-1 and through SFB 357). Computer time provided by the Höchstleistungsrechenzentrum Jülich, the Gesellschaft für wissenschaftliche Datenverarbeitung Göttingen, and the Regionales Hochschul-Rechenzentrum at Kaiserslautern is gratefully acknowledged. We thank Profs. H.-J. Werner (Universität Stuttgart) and P.J. Knowles (University of Birmingham) for providing us with various versions of MOLPRO. Financial support by the Fonds der chemischen Industrie is gratefully acknowledged.

References

1. Hayhurst AN, Kittelson DB (1978) Combust Flame 31:37
2. Gruebele M, Polak M, Saykally RJ (1987) J Chem Phys 87:1448
3. Meyer W (1971) Int J Quantum Chem Symp 5:341
4. Meyer W (1973) J Chem Phys 58:1017
5. Botschwina P (1987) J Chem Soc Faraday Trans II 84:1559
6. Botschwina P (1989) In: Maier JP (ed) Ion and cluster ion spectroscopy and structure. Elsevier, Amsterdam, pp 59–108
7. Ervin KM, Lineberger WC (1991) J Phys Chem 95:1167
8. Sebald P (1990) Dissertation, Kaiserslautern
9. Botschwina P, Sebald P (1991) In: Jennings KR (ed) Fundamentals of gas phase ion chemistry. Kluwer, Dordrecht, pp 231–233
10. Tian A, Cao Z, Zhang J, Yau G (1993) J Mol Struct (Theochem). 285:293
11. Seeger S (1995) Dissertation. Cuvillier-Verlag, Göttingen
12. Botschwina P, Schmatz S (1996) In: Baer T, Ng CY, Powis I (eds) The structure, energetics and dynamics of organic ions. Wiley, Chichester
13. Botschwina P, Seeger S, Mladenović M, Schulz B, Horn M, Schmatz S, Flügge J, Oswald R (1995) Int Rev Phys Chem 169:14
14. Raghavachari K, Trucks GW, Pople JA, Head-Gordon M (1989) Chem Phys Lett 157:479
15. Werner HJ, Knowles PJ, with contributions from Almlöf J, Amos RD, Deegan MJO, Elbert ST, Hampel C, Meyer W, Peterson KA, Pitzer R, Stone A, Taylor PR, Lindh R, Mura ME, Thorsteinsson T (MOLPRO: a package of ab initio programs)
16. Woon DE, Dunning TH Jr (1995) J Chem Phys 103:4572
17. Kendall RA, Dunning TH Jr, Harrison RJ (1992) J Chem Phys 96:6796
18. Carter S, Mills IM, Handy NC (1992) J Chem Phys 97:1606
19. Botschwina P, Oswald M, Flügge J, Heyl Ä, Oswald R (1993) Chem Phys Lett 209:117
20. Botschwina P, Horn M, Matuschewski M, Schick E, Sebald P (1997) J Mol Struct (Theochem) 400:119
21. Botschwina P (unpublished)
22. Eckart C (1935) Phys Rev 47:552
23. Watson JKG (1970) Mol Phys 19:465
24. Whitehead RJ, Handy NC (1975) J Mol Spectrosc 55:356
25. Sebald P (unpublished)
26. Landolt-Börnstein (1995) In: Guelachvilli G (ed) Group II vol 20, Molecular constants subvol b1 Gu Springer, Berlin, Heidelberg, New York
27. Maki A, Quapp W, Klee S, Mellau GC, Albert S (1996) J Mol Spectrosc 180:323
28. Carter S, Senekowitsch J, Handy NC, Rosmus P (1988) Mol Phys 65:143
29. Watson JKG (1987) J Mol Spectrosc 125:428
30. Purvis GD, Bartlett RJ (1982) J Chem Phys 76:1910
31. Hampel C, Peterson KA, Werner HJ (1997) Chem Phys Lett 99:9790
32. Deegan MJO, Knowles PJ (1994) Chem Phys Lett 227:321
33. Sutcliffe BT, Tennyson J (1986) Mol Phys 58:1053
34. (a) Mladenović M, Bačić Z (1990) J Chem Phys 93:3039; (b) Mladenović M, Bačić Z (1991) J Chem Phys 94:4988
35. Carter S, Handy NC (1986) Comput Phys Rep 5:115
36. Bačić Z, Light JC (1987) J Chem Phys 87:4008
37. Bačić Z (1991) J Chem Phys 95:3456
38. Schmatz S, Mladenović M (1997) Ber Bunsenges Phys Chem 101:372
39. Mladenović M, Schmatz S (1998) J Chem Phys 109:4456
40. Bowman JM, Gazdy B, Bentley JA, Lee TJ, Dateo CE (1993) J Chem Phys 99:308
41. Sutcliffe BT, Tennyson J (1986) Mol Phys 58:1053
42. Diehl H, Flügge S, Schröder U, Völkel A, Weiguny A (1961) Z Phys 162:1
43. Herzberg G (1945) Molecular spectra & molecular structure volII: infrared and Raman spectra of polyatomic molecules. Van Nostrand, New York
44. Kroto HW (1992) Molecular rotation spectra. Wiley, New York